

Article

Multiscale Interface Effect on Homogeneous Dielectric Structure of ZrO₂/Teflon Nanocomposite for Electrowetting Application

Jiaxin Hou^{1,2,†}, Yancong Feng^{1,2,†} , Jinglun Liao^{1,2,†}, Wenwen Ding^{1,2}, Lingling Shui^{1,2}, Hao Li^{1,2,*} , Yao Wang^{1,2}, Biao Tang^{1,2}, Ahmad Umar³ and Guofu Zhou^{1,2,4,5}

¹ Guangdong Provincial Key Laboratory of Optical Information Materials and Technology & Institute of Electronic Paper Displays, South China Academy of Advanced Optoelectronics, South China Normal University, Guangzhou 510006, China; houjiaxin1993@outlook.com (J.H.); fengyancong@m.scnu.edu.cn (Y.F.); liaojinglun@hotmail.com (J.L.); phoenix_wenwen@163.com (W.D.); shuill@m.scnu.edu.cn (L.S.); wangyao@m.scnu.edu.cn (Y.W.); tangbiao@scnu.edu.cn (B.T.); guofu.zhou@m.scnu.edu.cn (G.Z.)

² National Center for International Research on Green Optoelectronics, South China Normal University, Guangzhou 510006, China

³ Department of Chemistry, Faculty of Science and Arts and Promising Centre for Sensors and Electronic Devices, Najran University, Najran 11001, Saudi Arabia; ahmadumar786@gmail.com

⁴ Shenzhen Guohua Optoelectronics Tech. Co. Ltd., Shenzhen 518110, China

⁵ Academy of Shenzhen Guohua Optoelectronics, Shenzhen 518110, China

* Correspondence: haoli@scnu.edu.cn

† These authors contributed equally to this work.

Received: 6 September 2018; Accepted: 2 October 2018; Published: 9 October 2018



Abstract: Electrowetting-on-dielectric is a preferred option in practical applications of the electrowetting phenomenon but limited by dielectric and breakdown performances of the dielectric layer. In the present work, a ceramic/polymer nanocomposite as a novel dielectric layer is developed to intensify the overall electrowetting performances by multiscale interface effect. Hereinto, surface fluoro-modified ZrO₂ nanoparticles (mZrO₂) are dispersed well in AF 1600 matrix to form a mZrO₂@AF 1600 nanocomposite. The small addition of mZrO₂ improves the dielectric constant of the nanocomposite, and the experimental value is larger than the theoretical value calculated by Maxwell–Garnett model, but fits well with the Rahaman–Khastgir model. The molecular dynamics simulations with the explicit model further verify the interfacial effect. Meanwhile, double contact angle modulation and higher breakdown field strength (E_b) are obtained. For the three-layer sandwich structure, both the top and bottom AF 1600 layer decrease the surface roughness for better electrowetting reproducibility and wider wettability modulation. The Forlani–Minnaja theory related to the empirical relationship between E_b and thickness of dielectric layer fit well with the monolayer structure, but cannot be applied in multi-layer structures. A new relationship is proposed to guide the design of dielectric multi-layers with high breakdown field strength.

Keywords: electrowetting; dielectric layer; interface effect; ZrO₂ nanoparticles; Teflon

1. Introduction

Electrowetting is a microfluidic phenomenon that tunes the surface tension of the liquid droplet on the electrode to enable large and reversible contact angle variations via applied electric field [1,2]. Till now, it has grown into an efficient, versatile, and promising tool to regulate surface wettability of materials and shape of microdroplets, and been applied to electronic paper

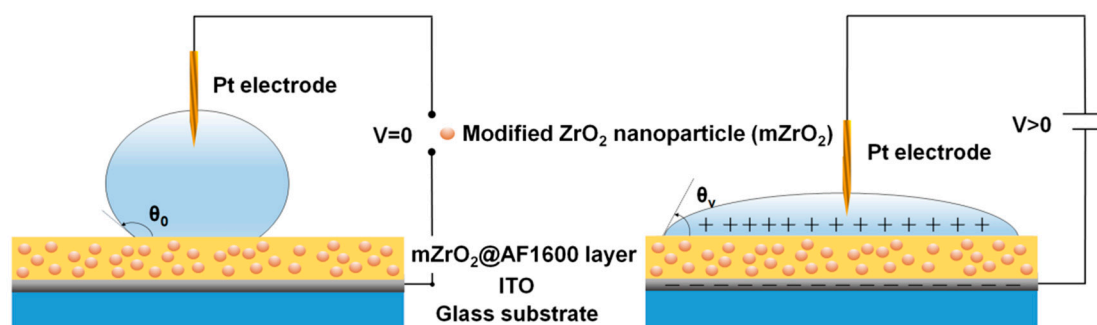
display [3], microfluidics [4,5], microlenses [6], fiber optics [7], and other electronic fields [8]. In these applications, electrowetting-on-dielectric (EWOD) is a preferred option more than direct electrowetting-on-a-conductor, by which a hydrophobic dielectric layer covers the electrode. High dielectric constant of layer material can strengthen the electrowetting effect in high electric fields. The resultant low surface energy and wettability can make surface microfluids flow expediently [9]. Thus, the dielectric layer is absolutely crucial to the overall performance of EWOD.

Nowadays, more and more inorganic or polymeric materials are used to present dielectric layers [10–12]. The former is good at high dielectric constant and low driving voltage, such as SiO_2 [13], Si_3N_4 [14], silicon nanosphere [15], and mesoporous silica [16]. However, their natural defects in film-processing ability seriously hinder the manufacture or electrowetting devices. In particular, high polarity of metal oxides (e.g., ZnO [17–19]) even causes incident dielectric lose efficiency. On the contrary, the latter represented as Teflon AF [20,21], Cytop TM [22], Parylene-C [23], polydimethylsiloxane [24], polyimide [25], poly(ethylene terephthalate)/polyethylene [26], and photoresist Su-8 [27], are mainly limited by their relatively low dielectric constant, which is adverse to decreasing driving voltage and avoiding dielectric breakdown [28].

Novel dielectric composite layers for EWOD are further developing, consisting of a top hydrophobic polymer layer and bottom dielectric inorganic/polymeric layer [29–32]. The layers combine the advantages of both inorganic and polymeric insulating materials but ignore the huge differences in chemical and physical properties between the two materials. Once an electric field is applied, electric charges inevitably concentrate on the surface of hydrophobic layer with much lower dielectric constant than the dielectric layer, accelerating the lose efficiency. In addition, their weak interlayer compatibility will cause layer-to-layer miss-registration, interstice, and even separation.

Addition of ceramic fillers can improve the dielectric constant of the composite. In particular, ferroelectric ceramics with perovskite structure, such as BaTiO_3 [33,34], possess intrinsic high dielectric constant up to hundreds and even thousands due to the spontaneous polarization. However, the polarization mainly concentrates upon the interior of fillers. The influence of fillers on the surface of material is still unclear. On the other hand, nanosized fillers are popular for the dielectric film with only sever micrometers; however, nanosized ferroelectric ceramic particles have relatively lower dielectric constant than bulk ceramics due to the phase transition from tetragonal to cubic [35]. For the devices of EWOD, the optical properties should be also considered, limiting the selectivity of type of filler.

As a consequence, we focus on integrating both inorganic and polymeric insulating materials into one highly compatible solution, and preparing the polymer nanocomposite. Within this composite structure, surface fluoro-modified zirconia (mZrO_2) nanoparticles with high dielectric constant [36] and high transmittance were hybridized into AF 1600 to form the dielectric nanocomposite. The electrowetting phenomenon of $\text{mZrO}_2/\text{AF 1600}$ nanocomposite is presented in Scheme 1. Under the electric field, the originally hydrophobic surface changes to be hydrophilic, leading to the decrease of contact angle of droplet on the surface.



Scheme 1. Schematic of electrowetting phenomenon of $\text{mZrO}_2/\text{AF 1600}$ nanocomposite.

Besides the dielectric constant, the breakdown field strength also plays a key role in the performance of dielectric materials. Designing sandwich-structured ceramic/polymer nanocomposites can significantly enhance breakdown field strength [37,38]. However, the relationship between multi-layer structure and breakdown field strength keeps confused. In the present work, sandwich structure is also designed for the enhancement of breakdown field strength, and the regularity is revealed. Meanwhile, the sandwich structure also avoids ionic polarization and alters the surface property.

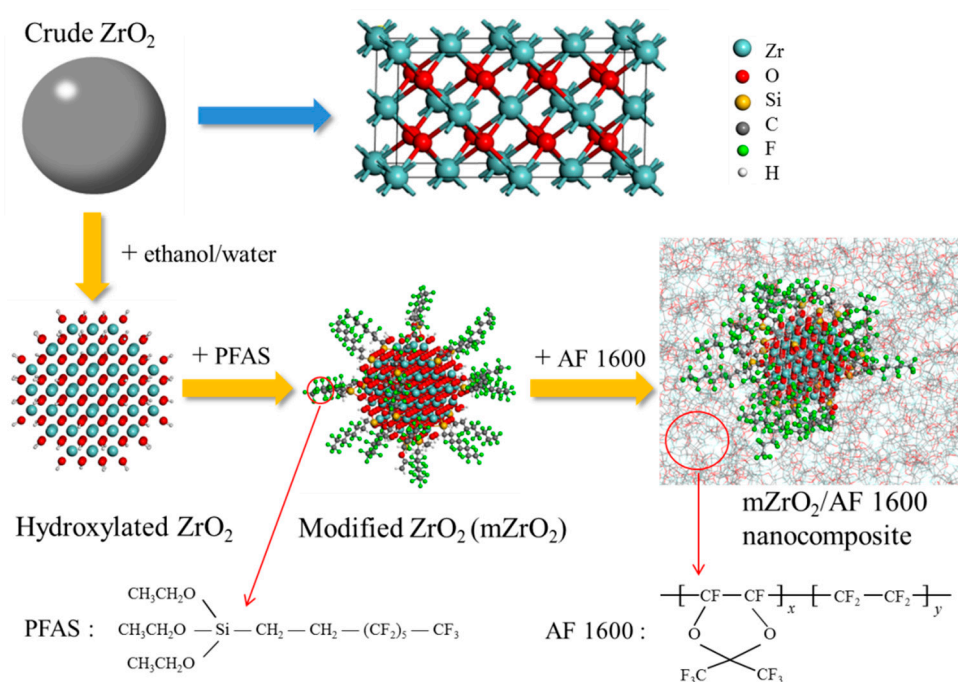
2. Experimental and Simulated Methods

2.1. Materials

ZrO₂ nanoparticles (99.9%; mean size: ~20 nm) and Teflon AF 1600 were purchased from Beijing DK nano technology Co., Ltd. (Beijing, China) and DuPont Company (Wilmington, DE, USA), respectively. 1H,1H,2H,2H-perfluorooctyltriethoxysilane (97%, J&KScientific Ltd., Beijing, China) and prefluorotributylamine (84%, Beijing HWRK Chem Co., Ltd., Beijing, China) were directly used without any further purification. Benzotrifluoride (99%, Adamas Reagent Co., Ltd., Shanghai, China) was dried by vacuum distillation over calcium hydride (CaH₂) prior to use. All other reagents are of analytic grade.

2.2. Surface Modification of ZrO₂ Nanoparticles

ZrO₂ nanoparticles were modified via surface coupling reaction of fluorinated silane coupling agent (see Scheme 2) as described in the literature [39]. Typically, the crude ZrO₂ nanoparticles were rinsed three times with acetone, ethanol and deionized water in ultrasonic cleaner for 10 min, respectively, and then were dried in vacuum at 60 °C for 12 h. In dry argon atmosphere, all these nanoparticles were mixed with 1H,1H,2H,2H-perfluorooctyltriethoxysilane at 1:1.5 mass mole⁻¹ ratio in benzotrifluoride by magnetic stirring at room temperature for 72 h. Finally, the mZrO₂ product was rinsed two times with ethanol and acetone, respectively, and then were dried in vacuum at 50 °C for 24 h.



Scheme 2. Schematic of preparation of mZrO₂/AF 1600 nanocomposite.

2.3. Characterization of ZrO₂ Nanoparticles

Scanning electron microscope (SEM): The morphologies of crude and modified ZrO₂ nanoparticles were observed using a ZEISS Ultra 55 (Germany) with the ions energy of 5 kV. Samples were respectively prepared by drying the ethanol solution of crude ZrO₂ and the benzotrifluoride solution of mZrO₂ with the same concentration of 0.1 mg mL⁻¹ on the clean glass flake adhered to the copper platform.

Static contact angle measurements: Two kinds of ZrO₂ nanoparticles were respectively tableted into plates using manual powder tablet press (769YP-15A, KEQI, Tianjin KEQI High & New Technology Corporation, Tianjin, China). Then, a 10 µL droplet of ultrapure water from a hydrophobized needle of a micro-syringe was dropped onto the surface of the plates. The resulting contact angle was recorded by a contact angle meter (JC2000C, POWEREACH, Shanghai, China), and measured by an image analysis software (DSA10Mk2 drop shape analysis system, Krüss Hamburg, Germany).

Fourier infrared spectrometer (FT-IR): The surface variation between the crude and modified ZrO₂ nanoparticles was identified by FT-IR (Tensor 27, Bruker, Karlsruhe, Germany) in a spectral range of 4000–400 cm⁻¹ with a resolution of 2 cm⁻¹ using a potassium bromide plate.

2.4. Compatibility Test of ZrO₂ with AF 1600

The compatibility tests were performed using differential scanning calorimetry (DSC; DSC1, METTLER TOLEDO, Zurich, Switzerland) within a temperature range of 25 to 200 °C at a heating rate of 10 °C min⁻¹ under nitrogen gas (flow rate: 10 mL min⁻¹).

2.5. Preparation on mZrO₂@AF 1600 Layer

Typically, a determined weight of mZrO₂ nanoparticles was uniformly dispersed in prefluorotributylamine solution of AF 1600 (3.7 wt %) by high intensity ultrasound (VCX150PB, SONICS, Newtown, PA, USA). Afterwards, the mixture was coated on the surface of indium tin oxide (ITO) glass using a spin coater (KW-4A, Institute of Microelectronics of the Chinese Academy of Sciences, Beijing, China) with a fixed rotating speed of 1200 rpm. Finally, the coated slide was dried in a vacuum at 100 °C for 2 h to remove the residual organic solvent thoroughly. Pure AF 1600 layer, double-, and three-layer structures were fabricated by repeating the same process.

2.6. Characterization of mZrO₂@AF 1600 Layer

Capacitor measurements: The capacitor measurements were performed by inputting signal of alternating current (AC; 0.5 V, 1 kHz) using an impedance analyzer (6500B, WAYNE KERR, London, UK). The positive pole of the impedance analyzer was attached to the platinum (Pt) probe that was inserted into a 10 µL droplet of 0.1 M sodium chloride (NaCl) aqueous solution on the layer surface, and the negative pole was attached to the ITO side of the substrate. The real-time capacity values were displayed on the screen of the impedance analyzer until remaining constant.

Surface profile analysis: The layer thickness, surface topography and roughness were measured by three-dimensional (3D) surface profiler (DCM8, Leica, Biberach, Germany) with a 50-fold objective.

Electrowetting test: The electrowetting tests were performed using digital regulated direct current (DC) power supply (CE0400010T, Earthworm Electronics, Shanghai, China) (see Scheme 1) with the same pole connection mentioned above in the capacitor measurements. As the applied voltage increased from 0 V to the breakdown voltage (V_b) value (see the following V_b measurements) with the step of 5 V, the real-time change of NaCl droplet was recorded by contact angle meter and analyzed using an image analysis software.

Dynamic contact angle measurements: Typically, a 10 µL droplet of ultrapure water from the hydrophobized needle of a micro-syringe was dropped onto the layer surface. During the movement of the objective table, the resulting advancing angle, and receding angle was recorded by contact angle meter, and measured by image analysis software.

V_b measurements: The V_b measurements were performed using a digital regulated DC power supply with the same pole connection mentioned above in the capacitor measurements. Along with increasing DC voltage, the real-time changes of NaCl droplet were observed by contact angle meter till a few tiny bubbles generated in the droplet. At this time, the applied DC voltage is viewed as V_b . The final V_b is the average of at least five measured values with mean square error less than 5 V.

2.7. Simulated Method

Scheme 2 shows the structure of Teflon AF. For the AF 1600, the ratio of x/y is 13/7. In our models, we built the AF 1600 molecules with $x = 13$ and $y = 7$. There were 100 molecules in the pure AF 1600 system. For the $m\text{ZrO}_2/\text{AF}$ 1600 nanocomposite, the spherical ZrO_2 (containing 87 Zr atoms and 174 O atoms) with a radius equaling to approximately 8 nm was built, and there were 100 AF 1600 molecules. The ZrO_2 particle was grafted by 20 PFAS molecules. The simulation was run at 500 K for 0.2 ns in the NPT ensemble to obtain sufficiently relaxed structures. Then, the system was run at 300 K in the NPT ensemble for 0.2 ns to obtain an equilibrated density. Finally, the simulation was run at 300 K in the NVT ensemble for 0.2 ns and the following 0.3 ns data were recorded for analysis.

3. Results and Discussion

As well-known, homogeneous nature is the prerequisite to optimize the overall performance of polymer composite, which is mainly determined by matrix compatibility. However, fluoropolymers represented as Teflon series is generally incompatible with other common materials. Therefore, “surface ligand engineering” is often introduced to improve the compatibility between filler and framework material [40,41]. Here we employed the coupling of 1H,1H,2H,2H-perfluorooctyltriethoxysilane (PFAS) to the hydroxylated surface of ZrO_2 nanoparticles to achieve surface fluorination (see Scheme 2).

In general, interfacial incompatibility exists due to the hydrophilicity of filler surface and hydrophobicity of polymer, leading to aggregation of nanoparticles [42,43]. Naturally, the introduced fluorocarbon chains [44] with a similar component as matrix chains will weaken the interaction within ZrO_2 nanoparticles against aggregation, just like what appears in Figure 1b. Here, there is no big aggregation of fluorosilane-modified nanoparticles ($m\text{ZrO}_2$), opposite to what the crude ZrO_2 ones did in Figure 1a. In particular, the static water contact angle rises from less than 10° to 135° , i.e., the superficial nature of the nanoparticles alters from hydrophilic to hydrophobic (see Figure 1c,d). It indicates that surface modification greatly changes the wettability of ZrO_2 . Moreover, the C–F stretching vibration ($1240\text{--}1100\text{ cm}^{-1}$), and Si–O antisymmetric stretching vibration (1070 cm^{-1}) in the FT-IR spectra (see Figure 2) also provide convincing evidence on surface fluorination.

Meanwhile, $m\text{ZrO}_2$ nanoparticles have a good compatibility with AF 1600 substrate. In the temperature transformation diagrams (Figure 3), crude AF 1600 exhibits two endothermic peaks, but only one peak after hybridization. Both glass transition temperature (T_g) and the specific heat capacity (ΔC_p) fall, along with the introduction of ZrO_2 and $m\text{ZrO}_2$ nanoparticles, respectively. Obviously, ZrO_2 particles with good thermal conductivity and high specific surface area can conduct heat rapidly and inhibit the intertwining of polymer molecular chains effectively as a result of the “easier” phase transition. Additionally, these surface-fluorinated $m\text{ZrO}_2$ particles further decrease T_g and ΔC_p of nanocomposites, which only attributes to their better compatibility with AF 1600 than ZrO_2 's. As previously mentioned, good matrix compatibility can lower the interfacial difference between nanofiller and framework material to make the nanocomposites more homogeneous. It will surely help tuning, even optimizing, some key functionalities for electrowetting intensification.

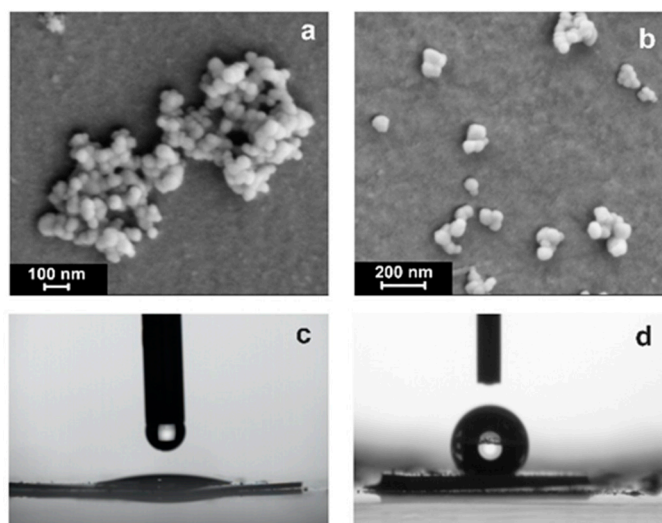


Figure 1. SEM and static water contact angle images of ZrO₂ nanoparticles before (a and c) and after surface fluorination (b and d), respectively.

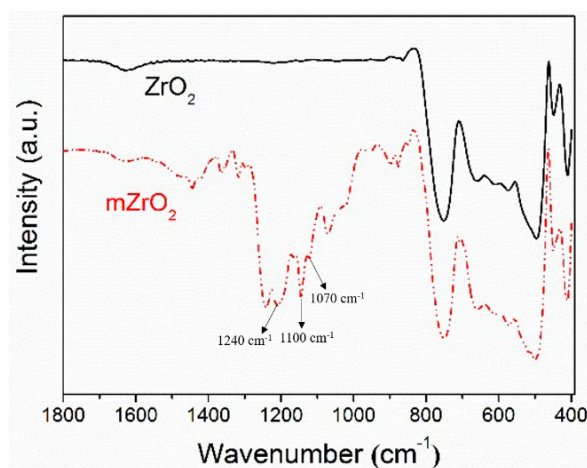


Figure 2. FT-IR spectra of crude zirconia (ZrO₂) and surface fluoro-modified zirconia (mZrO₂). The related peaks listed below: 1240–1100 cm⁻¹ (vs, C–F on PFAS) and 1070 cm⁻¹ (vas, Si–O linked with ZrO₂).

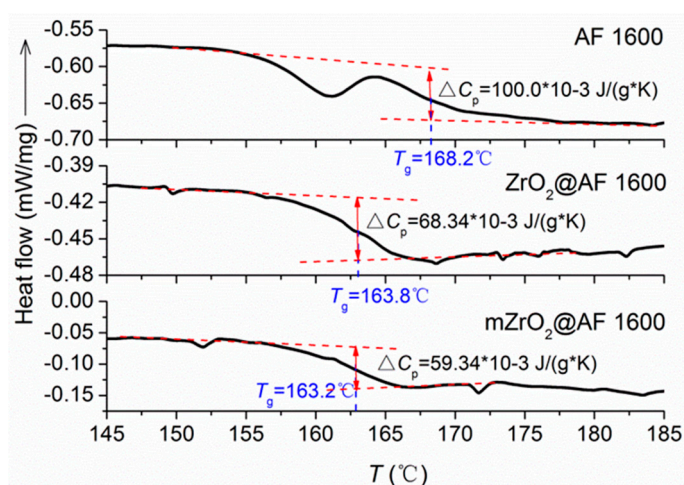


Figure 3. DSC heating curves of AF 1600, ZrO₂@AF 1600 and mZrO₂@AF 1600 samples (ΔC_p: the specific heat capacity).

In the EWOD device, the dielectric layer does perform as a capacitor blocking electron and hold large electrostatic energy. Once an electric potential is applied between the top and bottom electrode, an electric double layer will appear spontaneously both at the solid–liquid interface and the solid–solid interface to cause the originally hydrophobic layer surface to be hydrophilic. Hereinto, the ability of charge accumulation, or in a sense, the surface wettability variation, depends entirely on dielectric constant (ϵ) of the resulting insulating layer. In general, ϵ is obtained by calculation according to the following equation:

$$C = \epsilon\epsilon_0/t \tag{1}$$

where C is the capacitance per unit area, t is the thickness of the capacitor (i.e., dielectric layer between droplet and a solid electrode), ϵ_0 is the permittivity of free space which is approximately $8.85 \times 10^{-12} \text{ F m}^{-1}$.

Here, the obtained initial value of pure AF 1600 is only 1.54 that agrees with few measured data [45], but not with the general value (1.93). Just as shown in Figure 4, we investigated the relationship between ϵ value of $\text{mZrO}_2\text{@AF 1600}$ nanocomposite with mZrO_2 concentration in detail.

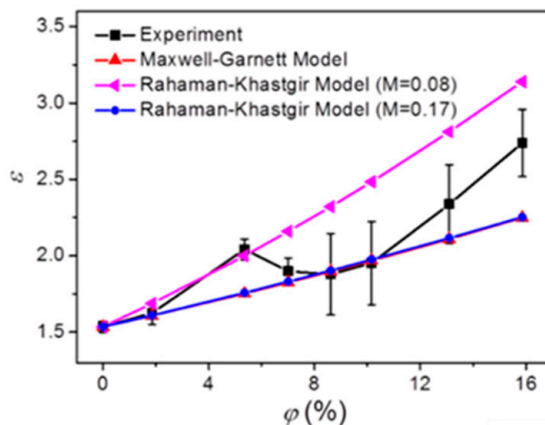


Figure 4. Experimental and theoretical dielectric constants (ϵ) of $\text{mZrO}_2\text{@AF 1600}$ nanocomposite films under different mZrO_2 volume fractions (ϕ).

The ϵ equaling to 2.02 at low volume fraction of mZrO_2 (5.35 vol %, i.e., 15 wt %) is higher than the theoretical value (1.75) calculated by Maxwell–Garnett model [46]:

$$\epsilon = \epsilon_m \frac{2\epsilon_m + \epsilon_f + 2\phi(\epsilon_f - \epsilon_m)}{2\epsilon_m + \epsilon_f - \phi(\epsilon_f - \epsilon_m)} \tag{2}$$

where ϕ represents the volume fraction of mZrO_2 in AF 1600 matrix, ϵ , ϵ_m and ϵ_f denote the dielectric constant of the $\text{mZrO}_2\text{@AF 1600}$ nanocomposite, AF 1600 matrix and mZrO_2 filler, respectively. The inconsistency between the theoretical and experimental values of ϵ maybe attribute to the neglecting of interfacial polarization in Maxwell–Garnett model.

On the contrary, the Rahaman–Khastgir model involving the effect of interfacial polarization fits well with experimental data [47]:

$$\log \epsilon = \log \epsilon_f + \frac{\log \epsilon_m - \log \epsilon_f}{e^{\frac{\phi}{M \cdot \log F}}} \tag{3}$$

where F is the measurement frequency (i.e., 1 kHz), and M is the morphological factor/fitting parameter, depending on shape, size, dispersion, distribution, and permittivity of particulate inclusion and host medium. It means that the improvement of dielectric constant at low mZrO_2 content attributes to the interfacial polarization.

For further understanding the interfacial effect of the composite, we adopted the molecular dynamics simulations with explicit atom model. Unlike the Tanaka's multi-core model [48] of polymer nanocomposite (including the bonded layer, bound layer and loose layer), there is no bound layer in the $m\text{ZrO}_2@AF\ 1600$ nanocomposite. The density of the matrix of composite is lower than that of pure AF 1600 ($1.98\ \text{g cm}^{-3}$ based on the MD's result), as shown in Figure 5. On the other hand, since the PFAS molecules do not cover the ZrO_2 particle, the bonded layer and the loose layer are overlapped. The interfacial region comprising of a bonded/loose layer possesses an ultralow density. Low density indicates high free volume where the orientation of dipole moment can be rearranged easily under the electric field. In other words, the orientational polarization in the interfacial region is greater than that in the matrix. Therefore, the poor packing would account for faster segmental and chain dynamics, i.e., the improvement of the dielectric constant [49].

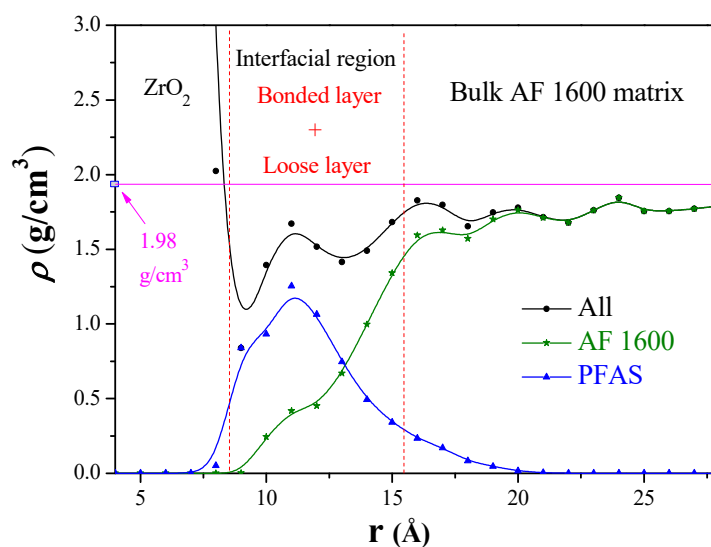


Figure 5. Density distribution around the center of ZrO_2 in the $m\text{ZrO}_2@AF\ 1600$ nanocomposite. The content of $m\text{ZrO}_2$ is 5 wt %, and the radius of $m\text{ZrO}_2$ is approximately 8 nm.

Given the above analyses, 5.35 vol % $m\text{ZrO}_2@AF\ 1600$ nanocomposite was chosen as the unique target of dielectric material to fabricate different dielectric layer structures in follow-up research. The surface morphology of dielectric film mainly decides the response rate and the reversibility of a droplet on the film under the applied electric field. Addition of inorganic fillers inevitably increases the surface roughness of organic polymer film. In Figure 6, the resulting $m\text{ZrO}_2@AF\ 1600$ film is almost as smooth as the AF 1600 one. Actually, its surface roughness ($R_a = 3.49\ \text{nm}$) is only slightly higher than the one of the latter ($R_a = 3.16\ \text{nm}$). Low surface roughness is attributed to low concentration and surface modification of inorganic fillers.

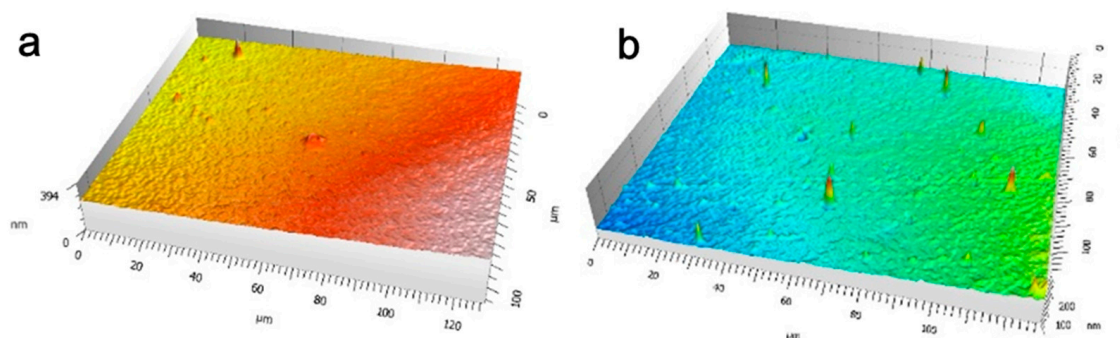


Figure 6. 3D surface topography of AF 1600 (a) and $m\text{ZrO}_2@AF\ 1600$ with 5.35 vol % $m\text{ZrO}_2$ (b) monolayer film under 50-fold objective.

After analyzing the dielectric constant and the surface roughness which are the crucial factors for the wettability, the contact angles are investigated. Figure 7a,c,d shows that, although the initial contact angle of the single $m\text{ZrO}_2@AF$ 1600 layer ($103^\circ \pm 1.5^\circ$) is lower than that of the AF 1600 layer ($114^\circ \pm 2.2^\circ$), its variation range of contact angles under applied DC electric field (17.8°) exceeds two times the AF 1600 one (8.2°). Very clearly, the larger contact angle modulation is based on higher dielectric constant of $m\text{ZrO}_2@AF$ 1600 nanocomposite according to the Young–Lippmann equation:

$$\cos \theta_v = \cos \theta_0 + \frac{1}{2\gamma} \varepsilon \varepsilon_0 U^2 \quad (4)$$

where θ_0 is the initial contact angle of droplet, θ_v is the contact angle under applied electric potential (U), γ is the surface tension between two immiscible fluids. However, its mildly wavy surface may bring about the drop of initial contact angle (see Figure 7a) and the rise of contact angle hysteresis (see Figure 7b). As the $m\text{ZrO}_2$ content rises, the dielectric layer becomes rougher to increase contact angle hysteresis against EWOD. Typically, the retreat ability and reproducibility of surface droplet will be weakened.

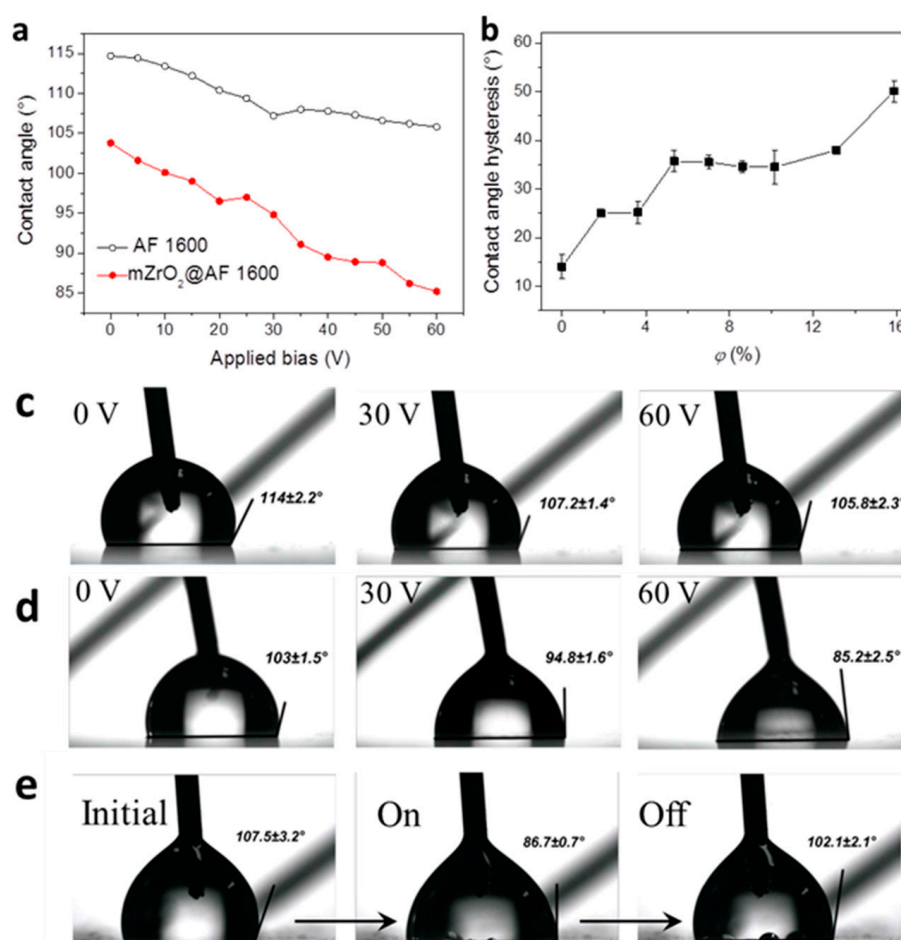


Figure 7. (a) Contact angles of the two films under applied DC electric field; (b) Contact angle hysteresis of the nanocomposite film with different $m\text{ZrO}_2$ concentrations; (c) Contact angle images of the monolayer AF 1600 and (d) $m\text{ZrO}_2@AF$ 1600 film at 0, 30 and 60 V, respectively; (e) Electrowetting reversibility of the sandwich structure.

It is also inevitable that some $m\text{ZrO}_2$ nanoparticles in the AF 1600 matrix next to the electrode substrate will be partially polarized by ionization. Therefore, we further developed a three-layer sandwich structure with a top and bottom pure AF 1600 layer, and a $m\text{ZrO}_2@AF$ 1600 interlayer,

to make up for the above defects. As presented in Figure 7e, if the voltage is on state, the difference of surface contact angle of the sandwich film (20.8°) is higher than that of the single AF 1600 layer (8.2°). Once the voltage changes to be off state, the difference between the initial contact angle and the recovered contact angle of the former is only 5.4° . Meanwhile, its driving-recovery process can work very rapidly and repeatedly. These results indicate that the sandwich structure containing $mZrO_2@AF$ 1600 layer possesses better electrowetting reversibility and wider wettability modulation. Apparently, the enhanced electrowetting reversibility is attributed to the reduced surface roughness based on the top AF 1600 layer, and the widened wettability variation is attributed to the increased dielectric constant based on the $mZrO_2@AF$ 1600 nanocomposite interlayer.

Besides surface wettability, both breakdown voltage and corresponding breakdown field strength (E_b) are considered as important evaluation indexes on the dielectric layer in EWOD. Based on the Young–Lippmann equation (Equation (4)), the E_b has a greater effect than ϵ on the contact angle modulation. Besides the nature of material, the thickness of the film has obvious influence on the breakdown field strength. According to the Forlani–Minnaja theory [50], the empirical relationship between E_b and thickness (t) appears as:

$$E_b \propto t^{-k} \quad (5)$$

where k is determined by the cooperation of lattice energy state, electron energy state and electron–lattice interaction. Therefore, we fabricated a series of monolayer $mZrO_2@AF$ 1600 and AF 1600 films with thickness varying from 0.12 to 1.70 μm for E_b analysis. As shown in Figure 8a, the $mZrO_2@AF$ 1600 layer exhibits higher E_b value than AF 1600's at the same thickness, similar to Dawber's [51] and Huang's [52] works on other amorphous solids. Obviously, it behaves with a higher proposed coefficient (79.53) and much closer to an ideal reciprocal relationship to t ($k = -0.98$). Here, the higher dielectric constant of the uniform nanocomposites originated from lack of ZrO_2 aggregation plays an important role at low turning concentration.

What is the function of the bottom AF 1600 layer? Besides the surface roughness, we also measured and analyzed the breakdown performances of double-layer composite structure and three-layer sandwich structure presented in Figure 8b,c. Obviously, the double-layer structure approximately obeys the basic principle of E_b that decreases followed by increasing layer thickness (see Figure 8a), but the sandwich structure does not, as shown in Figure 8b. In Figure 8c, the best fitting curves reveal that, E_b of the sandwich structure mainly depends on the determined thickness of both the $mZrO_2@AF$ 1600 interlayer and the bottom AF 1600 layer, and may be not affected by the top AF 1600 layer. Particularly, according to the fitting equation, high E_b is very possible to be obtained by rising t_n and falling t_b simultaneously. Additionally, the higher volume fraction of the $mZrO_2@AF$ 1600 interlayer (φ_n) and the resulting higher dielectric index (ϵ) also does. On the contrary, the opposite laws of layer thickness with ϵ and E_b (see Figure 8b,c) do not allow the double-layer composite structure to keep both ϵ and E_b gentle at a relatively high level for electrowetting intensification. Here, it is found that the bottom AF 1600 layer is of decisive importance in the three-layer sandwich structure. Just as mentioned previously, inorganic metal oxide with high polarity is very easily ionically polarized as a result of dielectric lose efficiency, but the bottom AF 1600 layer prevents its occurrence.

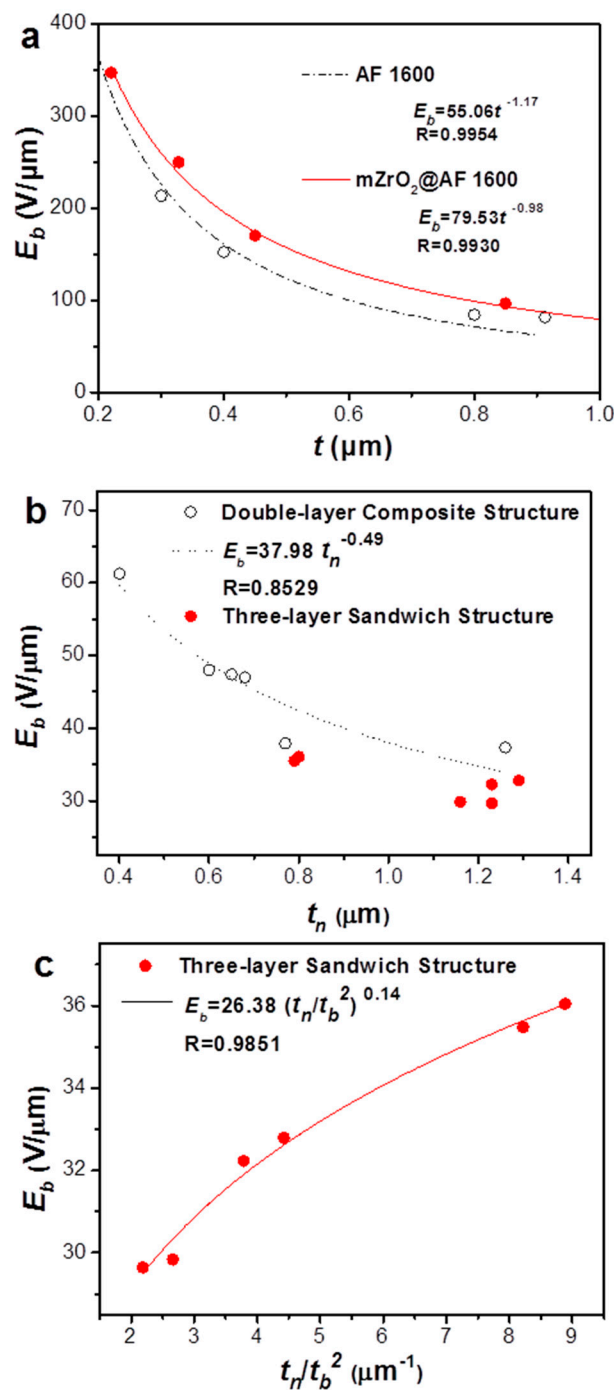


Figure 8. Mathematical relationship between thickness and breakdown field strength (E_b) of (a) monolayer AF 1600 and mZrO₂@AF 1600 film; (b) double-layer and (c) three-layer, respectively. Note that, t is total thickness, t_n is thicknesses of the mZrO₂@AF 1600 layer (mZrO₂ content: 5.35 vol %) and t_b is the thicknesses of the bottom AF 1600 layer.

4. Conclusions

In conclusion, in order to optimize the dielectric performances of the insulating layer in EWOD, we combined theoretical models, molecular dynamics simulations, and experimental methods. In the experiments, we fabricated a polymer nanocomposite that combines the advantages of inorganic materials, fluoropolymer, and organic/inorganic composite structure. Here, the interfacial effect plays an important and conclusive role in outstanding electrowetting intensification. Firstly,

surface-fluorinated modification of ZrO₂ nanoparticles improves the compatibility of nanoparticles and the AF 1600 matrix to increase the dielectric constant of mZrO₂@AF 1600 nanocomposite (2.02, about 31% higher than pure AF 1600's) at low content, followed by double contact angle modulation and higher breakdown field strength. The small addition of mZrO₂ improves the dielectric constant of the nanocomposite, and the experimental value is larger than the theoretical value calculated by the Maxwell–Garnett model, but fits well with the Rahaman–Khastgir model. The molecular dynamics simulations with the explicit model further verifies the interfacial effect.

Its only weakness is that the nanoparticle hybridization surely generates worse contact angle hysteresis. In the sandwich structure, both the top and bottom AF 1600 layer may weaken the bumpy medial mZrO₂@AF 1600 layer for better electrowetting reversibility and wider wettability modulation. At the same time, the bottom layer isolated those ZrO₂ nanoparticles from the electrode against ionic polarization. Marvelously, this structure can change the relationship between volume fraction of mZrO₂@AF 1600 layer and E_b , which will make more potential spaces for overall enhancements on both dielectric and breakdown performances. Multiscale interface effects based on the surface modification of nanoparticles and design of sandwich structure are revealed. It is anticipated to provide a facile, effective and practical strategy for enhancing the electrowetting performances of EWOD.

Author Contributions: H.L. conceived and designed the experiments; J.H., J.L. and W.D. performed the experiments; Y.F. and J.L. performed the simulations and analyzed the data; L.S., Y.W., A.U., and B.T. provided some suggestions for this project; H.L., Y.F., and J.H. wrote the manuscript; J.L. and G.Z. helped us to revise the manuscript. All authors critically reviewed the manuscript.

Funding: This work was financially supported by the National Key Research and Development Program of China (No. 2016YFB0401501), National Natural Science Foundation of China (No. 51703070), Key Cultivation Project of Basic Research of Guangdong Natural Science Foundation (No. 2014A030308013), Guangdong Provincial Key Laboratory of Optical Information Materials and Technology (No. 2017B030301007), MOE International Laboratory for Optical Information Technologies and the 111 Project, and Guangzhou Municipal Key Laboratory of Electronic Paper Displays Materials and Devices (No. 201705030007).

Acknowledgments: This work was technically supported by the Chemcloudcomputing of the Beijing University of Chemical Technology.

Conflicts of Interest: The authors declare no conflict of interest.

References

1. Mugele, F.; Baret, J.-C. Electrowetting: from basics to applications. *J. Phys. Condens. Matter* **2005**, *17*, R705–R774. [[CrossRef](#)]
2. Xia, Y.; Chen, J.; Zhu, Z.; Zhang, Q.; Yang, H.; Wang, Q. Significantly enhanced dielectric and hydrophobic properties of SiO₂@MgO/PMMA composite films. *RSC Adv.* **2018**, *8*, 4032–4038. [[CrossRef](#)]
3. Hayes, R.A.; Feenstra, B.J. Video-speed electronic paper based on electrowetting. *Nature* **2003**, *425*, 383–385. [[CrossRef](#)] [[PubMed](#)]
4. Kong, T.; Brien, R.; Njus, Z.; Kalwa, U.; Pandey, S. Motorized actuation system to perform droplet operations on printed plastic sheets. *Lab Chip* **2016**, *16*, 1861–1872. [[CrossRef](#)] [[PubMed](#)]
5. Gao, J.; Chen, T.; Dong, C.; Jia, Y.; Mak, P.I.; Vai, M.I.; Rui, P.M. Adhesion promoter for a multi-dielectric-layer on a digital microfluidic chip. *RSC Adv.* **2015**, *5*, 48626–48630. [[CrossRef](#)]
6. Terrab, S.; Watson, A.M.; Roath, C.; Gopinath, J.T.; Bright, V.M. Adaptive electrowetting lens-prism element. *Opt. Express* **2015**, *23*, 25838–25845. [[CrossRef](#)] [[PubMed](#)]
7. Ozbay, B.N.; Losacco, J.T.; Cormack, R.; Weir, R.; Bright, V.M.; Gopinath, J.T.; Restrepo, D.; Gibson, E.A. Miniaturized fiber-coupled confocal fluorescence microscope with an electrowetting variable focus lens using no moving parts. *Opt. Lett.* **2015**, *40*, 2553–2556. [[CrossRef](#)] [[PubMed](#)]
8. Khan, I.; Castelletto, S.; Rosengarten, G. Fabrication of solar beam steering electrowetting devices—present status and future prospects. *J. Phys. D Appl. Phys.* **2017**, *50*, 403001. [[CrossRef](#)]
9. Nelson, W.C.; Kim, C.-J.C. Droplet Actuation by Electrowetting-on-Dielectric (EWOD): A Review. *J. Adhes. Sci. Technol.* **2012**, *26*, 1747–1771. [[CrossRef](#)]
10. Liu, H.; Dharmatilleke, S.; Maurya, D.K.; Tay, A.A.O. Dielectric materials for electrowetting-on-dielectric actuation. *Microsyst. Technol.* **2010**, *16*, 449–460. [[CrossRef](#)]

11. Li, Z.; Haigh, A.; Soutis, C.; Gibson, A.; Sloan, R. Dielectric constant of a three-dimensional woven glass fibre composite: Analysis and measurement. *Compos. Struct.* **2017**, *180*, 853–861. [[CrossRef](#)]
12. Bormashenko, E.; Pogreb, R.; Bormashenko, Y.; Aharoni, H.; Shulzinger, E.; Grinev, R.; Rozenman, D.; Rozenman, Z. Progress in low voltage reversible electrowetting with lubricated polymer honeycomb substrates. *RSC Adv.* **2015**, *5*, 32491–32496. [[CrossRef](#)]
13. Lapiere, F.; Brunet, P.; Coffinier, Y.; Thomy, V.; Blossey, R.; Boukherroub, R. Simulations of theoretically informed coarse grain models of polymeric systems. *Faraday Discuss.* **2010**, *146*, 125–139. [[CrossRef](#)] [[PubMed](#)]
14. Shen, H.H.; Chung, L.Y.; Yao, D.J. Improving the dielectric properties of an electrowetting-on-dielectric microfluidic device with a low-pressure chemical vapor deposited Si₃N₄ dielectric layer. *Biomicrofluidics* **2015**, *9*, 022403. [[CrossRef](#)] [[PubMed](#)]
15. Mats, L.; Bramwell, A.; Dupont, J.; Liu, G.; Oleschuk, R. Electrowetting on superhydrophobic natural (Colocasia) and synthetic surfaces based upon fluorinated silica nanoparticles. *Microelectron. Eng.* **2015**, *148*, 91–97. [[CrossRef](#)]
16. Ghazzal, M.N.; Joseph, M.; Kebaili, H.; De Coninck, J.; Gagneaux, E.M. Tuning the selectivity and sensitivity of mesoporous dielectric multilayers by modifying the hydrophobic–hydrophilic balance of the silica layer. *J. Mater. Chem.* **2012**, *22*, 22526–22532. [[CrossRef](#)]
17. Kudr, J.; Richtera, L.; Nejd, L.; Xhaxhiu, K.; Vitek, P.; Rutkay-Nedecky, B.; Hynek, D.; Kopel, P.; Adam, V.; Kizek, R. Improved electrochemical detection of zinc ions using electrode modified with electrochemically reduced graphene oxide. *Materials* **2016**, *9*, 31. [[CrossRef](#)] [[PubMed](#)]
18. Wu, J.; Xia, J.; Lei, W.; Wang, B.P. Electrowetting on ZnO nanowires. *Appl. Phys. A* **2010**, *99*, 931–934. [[CrossRef](#)]
19. Papadopoulou, E.L.; Pagkozidis, A.; Barberoglou, M.; Fotakis, C.; Stratakis, E. Electrowetting properties of ZnO and TiO₂ nanostructured thin films. *J. Phys. Chem. C* **2010**, *114*, 10249–10253. [[CrossRef](#)]
20. Bienia, M.; Catherine Quilliet, A.; Vallade, M. Modification of drop shape controlled by electrowetting. *Langmuir* **2003**, *19*, 9328–9333. [[CrossRef](#)]
21. Welters, W.J.J.; Fokink, L.G.J. Fast electrically switchable capillary effects. *Langmuir* **1998**, *14*, 1535–1538. [[CrossRef](#)]
22. Banpurkar, A.; Sawane, Y.B.; Wadhai, S.M.; Murade, C.; Siretanu, I.; van den Ende, D.; Mugele, F. Using one halogen bond to change the nature of a second bond in ternary complexes with P · · · Cl and F · · · Cl halogen bonds. *Faraday Discuss.* **2017**, *199*, 29–47. [[CrossRef](#)] [[PubMed](#)]
23. Burger, B.; Rabot, R. Design of low hysteresis electrowetting systems in non-aqueous media by the addition of low HLB amphiphilic compounds. *Colloids Surfaces A* **2016**, *510*, 129–134. [[CrossRef](#)]
24. Tamaddoni, N.; Taylor, G.; Hepburn, T.; Michael, K.S.; Sarles, S.A. Reversible, voltage-activated formation of biomimetic membranes between triblock copolymer-coated aqueous droplets in good solvents. *Soft Matter* **2016**, *12*, 5096–5109. [[CrossRef](#)] [[PubMed](#)]
25. Kopp, D.; Zappe, H. Tubular astigmatism-tunable fluidic lens. *Opt. Lett.* **2016**, *41*, 2735–2738. [[CrossRef](#)] [[PubMed](#)]
26. Xiao, K.; Zhou, Y.; Kong, X.Y.; Xie, G.; Li, P.; Zhang, Z.; Wen, L.; Jiang, L. Electrostatic-charge- and Electric-field-induced smart gating for water transportation. *ACS Nano* **2016**, *10*, 9703–9709. [[CrossRef](#)] [[PubMed](#)]
27. Kumar, V.; Sharma, N.N. SU-8 as hydrophobic and dielectric thin film in electrowetting-on-dielectric based microfluidics device. *J. Nanotech.* **2012**, 312784. [[CrossRef](#)]
28. Facchetti, A.M.; Yoon, H.; Marks, T.J. Gate Dielectrics for organic field-effect transistors: new opportunities for organic electronics. *Adv. Mater.* **2005**, *17*, 1705–1725. [[CrossRef](#)]
29. Koumoulos, E.P.; Charitidis, C.A.; Papageorgiou, D.P.; Papatheanasiou, A.G.; Boudouvis, A.G. Nanomechanical and nanotribological properties of hydrophobic fluorocarbon dielectric coating on tetraethoxysilane for electrowetting applications. *Surf. Coat. Technol.* **2012**, *206*, 3823–3831. [[CrossRef](#)]
30. Khodayari, M.; Hahne, B.; Crane, N.B.; Volinsky, A.A. Floating electrode electrowetting on hydrophobic dielectric with an SiO₂ layer. *Appl. Phys. Lett.* **2013**, *102*, 192907. [[CrossRef](#)]
31. Schultz, A.; Chevalliot, S.; Kuiper, S.; Heikenfeld, J. Detailed analysis of defect reduction in electrowetting dielectrics through a two-layer ‘barrier’ approach. *Thin Solid Films* **2013**, *534*, 348–355. [[CrossRef](#)]

32. Jiang, C.; Ma, H.; Hasko, D.G.; Nathan, A. Influence of polarization on contact angle saturation during electrowetting. *Appl. Phys. Lett.* **2016**, *109*, 211601. [[CrossRef](#)]
33. Zhang, X.; Shen, Y.; Zhang, Q.; Gu, L.; Hu, Y.; Du, J.; Lin, Y.; Nan, C.W. Ultrahigh Energy Density of Polymer Nanocomposites Containing BaTiO₃@TiO₂ Nanofibers by Atomic-Scale Interface Engineering. *Adv. Mater.* **2015**, *27*, 819. [[CrossRef](#)] [[PubMed](#)]
34. Dang, Z.M.; Yuan, J.K.; Yao, S.H.; Liao, R.J. Flexible nanodielectric materials with high permittivity for power energy storage. *Adv. Mater.* **2013**, *25*, 6334–6365. [[CrossRef](#)] [[PubMed](#)]
35. Zhang, X.; Li, B.-W.; Dong, L.; Liu, H.; Chen, W.; Shen, Y.; Nan, C.-W. Superior Energy Storage Performances of Polymer Nanocomposites via Modification of Filler/Polymer Interfaces. *Adv. Mater. Interf.* **2018**, *5*, 1800096. [[CrossRef](#)]
36. Beaulieu, M.R.; Baral, J.K.; Hendricks, N.R.; Tang, Y.; Briseno, A.L.; Watkins, J.J. Solution processable high dielectric constant nanocomposites based on ZrO₂ nanoparticles for flexible organic transistors. *ACS Appl. Mater. Interfaces* **2013**, *5*, 13096–13103. [[CrossRef](#)] [[PubMed](#)]
37. Hu, P.; Shen, Y.; Guan, Y.; Zhang, X.; Lin, Y.; Zhang, Q.; Nan, C.W. Topological-Structure Modulated Polymer Nanocomposites Exhibiting Highly Enhanced Dielectric Strength and Energy Density. *Adv. Funct. Mater.* **2014**, *24*, 3172–3178. [[CrossRef](#)]
38. Wang, Y.; Cui, J.; Wang, L.; Yuan, Q.; Niu, Y.; Chen, J.; Wang, Q.; Wang, H. Compositional tailoring effect on electric field distribution for significantly enhanced breakdown strength and restrained conductive loss in sandwich-structured ceramic/polymer nanocomposites. *J. Mater. Chem. A* **2017**, *5*, 4710–4718. [[CrossRef](#)]
39. Kujawa, J.; Cerneaux, S.; Kujawski, W. Characterization of the surface modification process of Al₂O₃, TiO₂ and ZrO₂ powders by PFAS molecules. *Colloids Surfaces A* **2014**, *447*, 14–22. [[CrossRef](#)]
40. Li, Y.; Krentz, T.M.; Wang, L.; Benicewicz, B.C.; Schadler, L.S. Ligand engineering of polymer nanocomposites: From the simple to the complex. *ACS Appl. Mater. Interfaces* **2014**, *6*, 6005–6021. [[CrossRef](#)] [[PubMed](#)]
41. Özden-Yenigün, E.; Bilge, K.; Sünbuloğlu, E.; Bozdağ, E.; Papila, M. High strain rate response of nanofiber interlayered structural composites. *Compos. Struct.* **2017**, *168*, 47–55. [[CrossRef](#)]
42. Kango, S.; Kalia, S.; Celli, A.; Njuguna, J.; Habibi, Y.; Kumar, R. Surface modification of inorganic nanoparticles for development of organic–inorganic nanocomposites—A review. *Prog. Polym. Sci.* **2013**, *38*, 1232–1261. [[CrossRef](#)]
43. Iijima, M.; Kamiya, H. Surface modification for improving the stability of nanoparticles in liquid media. *KONA Powder Part. J.* **2009**, *27*, 119–129. [[CrossRef](#)]
44. Lemal, D.M. Perspective on fluorocarbon chemistry. *J. Org. Chem.* **2004**, *69*, 1–11. [[CrossRef](#)] [[PubMed](#)]
45. Ding, S.J.; Wang, P.F.; Zhang, D.W.; Wang, J.T.; Wei, W.L. A novel structural amorphous fluoropolymer film with an ultra-low dielectric constant. *Mater. Lett.* **2001**, *49*, 154–159. [[CrossRef](#)]
46. Maxwell-Garnett, J.C. Colours in metal glasses and in metallic films. *Philos. Trans. R. Soc. A* **1904**, *203*, 385–420. [[CrossRef](#)]
47. Rahaman, M.; Chaki, T.K.; Khastgir, D. Consideration of interface polarization in the modeling of dielectric property for ethylene vinyl acetate (EVA)/polyaniline conductive composites prepared through in-situ polymerization of aniline in EVA matrix. *Eur. Polym. J.* **2012**, *48*, 1241–1248. [[CrossRef](#)]
48. Tanaka, T.; Kozako, M.; Fuse, N.; Ohki, Y. Proposal of a multi-core model for polymer nanocomposite dielectrics. *IEEE Trans. Dielect. Electr. Insul.* **2005**, *12*, 669–681. [[CrossRef](#)]
49. Casalini, R.; Roland, C.M. Local and global dynamics in polypropylene glycol/silica composites. *Macromolecules* **2016**, *49*, 3919–3924. [[CrossRef](#)]
50. Forlani, F.; Minnaja, N. Thickness influence in breakdown phenomena of thin dielectric films. *Phys. Status Solidi* **1964**, *4*, 311–324. [[CrossRef](#)]
51. Dawber, M.; Rabe, K.M.; Scott, J.F. Critical adsorption at the free surface of a smectic liquid crystal possessing a second-order phase transition. *Rev. Mod. Phys.* **2005**, *77*, 1083–1130. [[CrossRef](#)]
52. Huang, J.; Shian, S.; Diebold, R.M.; Suo, Z.; Clarke, D.R. The thickness and stretch dependence of the electrical breakdown strength of an acrylic dielectric elastomer. *Appl. Phys. Lett.* **2012**, *101*, 122905. [[CrossRef](#)]

